International Forum on Aeroelasticity and Structural Dynamics
IFASD 2022
13-17 June 2022, Madrid, Spain

INFLUENCE OF LAMINARITY ON THE AEROELASTIC BEHAVIOR OF THE NLR7301 AIRFOIL

Marc Braune[1], **Holger Mai**[1], **Anne Hebler**[1]

[1]German Aerospace Center (DLR), Institute of Aeroelasticity,
Bunsenstraße 10, 37073 Göttingen, Germany
Marc.Braune@dlr.de
Holger.Mai@dlr.de
Anne.Hebler@dlr.de

Keywords: flutter, aeroelastic instability, laminarity, boundary layer transition, laminar airfoil

Abstract: Aerodynamic and aeroelastic investigations on the CAST 10-2 laminar airfoil have shown an essential influence of laminarity on the aeroelastic behavior. To generalize these results, another transonic flutter test was performed with the supercritical NLR7301 airfoil, which demonstrates comparable laminar airfoil properties for Reynolds-numbers around $\mathrm{Re}_\infty = 2 \cdot 10^6$. Specific test runs with a free and a fixed boundary layer transition were performed to evaluate the influence of laminarity.

The results of the flutter test show that comparable aerodynamic and aeroelastic effects occur on the NLR701 airfoil as previously described for the CAST 10-2 airfoil. Thus, aerodynamic nonlinearities with large gradients as well as unsteady effects occur for a free boundary layer transition, some of which are reflected in aerodynamic limit cycle oscillations. A shift of the transonic dip towards lower total pressures for a free boundary layer transition is observed. An influence of the boundary layer state on the buffeting boundary is also indicated. In addition, aeroelastic instabilities were also observed for the NLR7301 supercritical airfoil, showing strong similarities to boundary layer transition flutter cases as described for the CAST 10-2 laminar airfoil.

The results confirm that laminar or turbulent boundary layer flows lead to different aeroelastic behavior. The results for the NLR7301 airfoil complement the previous results for the CAST 10-2 airfoil, generalize them and exclude airfoil-specific effects. The need for consideration of a free boundary layer transition in aeroelastic risk assessment is thus confirmed and reinforced.

1 INTRODUCTION

In the past, the influence of laminarity or the behavior of the boundary layer was hardly considered in the evaluation of aeroelastic risks of airfoils. Numerical as well as experimental investigations within the framework of a long-term strategy of the German Aerospace Center - Institute of Aeroelasticity (DLR-AE) [1] have clearly shown, however, that under specific boundary conditions the laminar-turbulent boundary layer transition can have a decisive influence on the aeroelastic behavior of airfoils.

Extensive investigations on the supercritical CAST 10-2 laminar airfoil have shown that the laminar-turbulent boundary layer transition strongly influences the aerodynamics [2, 3]. This was reflected in pronounced nonlinearities of the steady as well as the unsteady aerodynamic coefficients. Such nonlinearities were also found in the aeroelastic behavior. In addition to limit cycle oscillations (LCOs), the occurrence of self-excited flutter oscillations is described by subcritical bifurcations and hysteresis [3–6], among others. Furthermore, the aeroelastic stability limit also depends on the state of the boundary layer. For a free transitional boundary layer, the transonic dip of the CAST 10-2 laminar airfoil becomes deeper. It shifts to smaller Mach-numbers and lower total pressures compared to a fully turbulent one [4,7,8]. Moreover, for specific boundary conditions, new aeroelastic effects related to the motion of the laminar-turbulent boundary layer transition arise. These effects have recently been identified as boundary layer transition flutter and boundary layer transition buffet [9].

Nonlinear aeroelastic phenomena also appear on the supercritical NLR7301 airfoil, as confirmed by previous flutter tests [10–12]. Characteristics of a laminar airfoil were also found for the NLR7301 airfoil in previous investigations, so that comparable effects of the boundary layer transition on the aeroelastic behavior could be assumed for this airfoil as well.

In a transonic flutter test, the influence of laminarity on the aerodynamic and aeroelastic behavior of the NLR7301 airfoil has now been systematically investigated for the first time. It is shown that in a laminar or transitional boundary layer flow, in addition to the aerodynamic nonlinearities, a shift of the transonic dip to smaller total pressures occurs. Furthermore, aeroelastic instabilities occur solely for a free boundary layer transition, which show analogies to novel flutter and buffet phenomena as described for the first time for the CAST 10-2 laminar airfoil.

The following paper will provide an overview of the flutter test, describe the effects that arise, and discuss the aerodynamic as well as aeroelastic relationships. The paper will further illustrate the need to include laminar-turbulent boundary layer transition in a full aeroelastic system assessment.

2 EXPERIMENTAL METHODOLOGY

The presented results were obtained by a 2D flutter experiment on a NLR7301 supercritical airfoil model performed in the Transonic Wind Tunnel Göttingen (DNW-TWG) using the flutter test rig of DLR-AE. The experimental setup is described below.

2.1 Wind tunnel and flutter test rig

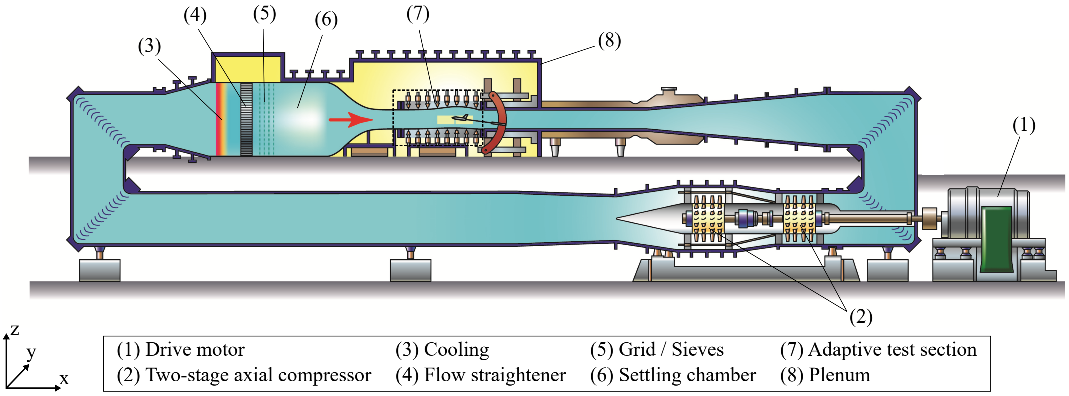

Figure 1: Schematic illustration of the DNW-TWG with the adaptive test section, modified according to internal communication with DNW. With respect to the coordinate system, the inflow is along the x-axis.

Fig. 1 shows a schematic representation of the DNW-TWG. The wind tunnel is operated by the German-Dutch Wind Tunnel Foundation (DNW) and is located on the DLR site in Göttingen.

The experiment itself was performed in the adaptive test section (dimensions: 1 m×1 m×4.5 m). Adaptive lower and upper walls were used to provide a two-dimensional adaptation to the steady flow field in order to minimize wall-induced disturbances [13]. With this setup, Mach-numbers Ma_∞ in the range $0.3 \leq \mathrm{Ma}_\infty \leq 0.9$ can be realized. The evacuation or pressurization of the entire wind tunnel plenum further allows the variation of the total pressure p_0 from 30 kPa up to 150 kPa, which is also accompanied by a change in the Reynolds-number Re_∞. Mach-number control is possible within a step size of order of $\mathcal{O}(10^{-3})$, while measurement accuracy is above this with an error of $\sigma_{\mathrm{Ma}_\infty} < \mathcal{O}(10^{-3})$.

Into the adaptive test section the 2D-support of the DNW-TWG was integrated, in which in turn the flutter test rig was installed. The support allows a rotation of the whole test rig including the wind tunnel model by an angle α_{2D} to realize an adjustment of the mean angle of attack α_0 around an aeroelastic equilibrium. The setup of the flutter test rig itself is shown in Fig. 2.

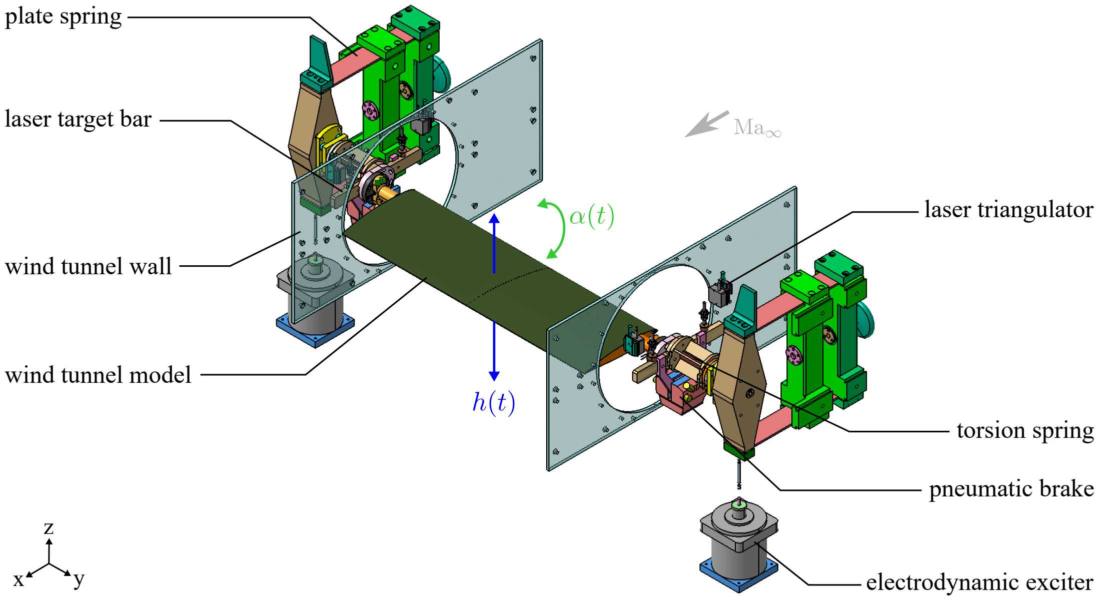

Figure 2: Schematic representation of the flutter test rig, the main components are labeled.

Designed for 2D wind tunnel tests, the test rig is composed of two opposing, identical spring systems. Each of these spring systems consists of plate springs and a torsion spring joint. The systems are located outside the wind tunnel walls and are connected in parallel via the wind tunnel model. The elastic model suspension provides a classical bending-torsion flutter system with the two rigid-body degrees of freedom (DoF) in heave $h(t)$ and pitch $\alpha(t)$. The motion of the airfoil model was measured by four laser triangulators (cf. Sec. 2.3). A beam directly connected to the wind tunnel model served as a laser target. A pneumatic friction brake acted as a safety system during the flutter tests and was also used to fix the model at a constant angle of attack. This allowed steady aerodynamic force and moment measurements to be made using the same experimental setup. As an additional safety mechanism, a flutter control system was used. Two electrodynamic exciters, connected to the plate springs, were controlled by a digital signal processor device (DSPS), which processed signals from the laser triangulators in real time. Flutter control could be used to excite the wind tunnel model, damp it completely, or control the oscillation amplitude. In addition, the system allows experimental bifurcation analysis. An amplitude-controlled excitation enables the selective detection of subcritical bifurcations.

2.2 NLR7301 wind tunnel model

The subject of the investigations was a supercritical NLR7301 airfoil model, which had already been used in a previous flutter test [12]. The geometry and the position of the pressure sensors are depicted in Fig. 3.

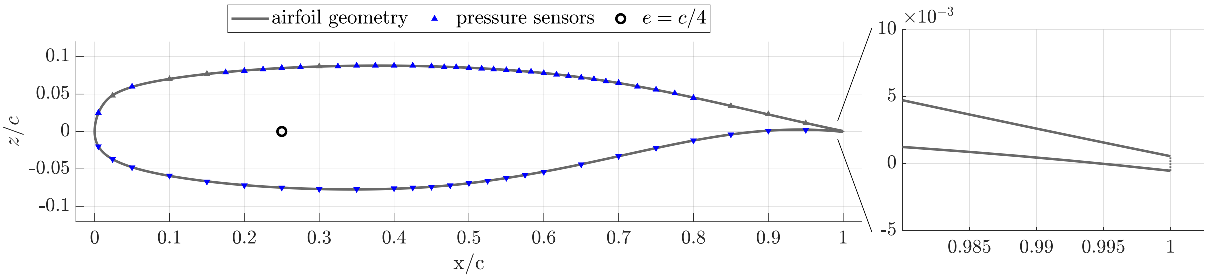

Figure 3: Airfoil contour and position of the pressure sensors of the NLR7301 wind tunnel model. In addition, the trailing edge is shown enlarged to visualize the truncate at $x/c = 1$.

The contour of the wind tunnel model corresponds largely to the geometry of the NLR7301 profile given by [14]. Differently, the trailing edge was truncated at $x/c = 1$, resulting in a blunt trailing edge with a thickness of about 0.1 % of the chord. This situation is shown in Fig. 3, resulting in a decreased camber of the airfoil and a reduction of the angle of incidence, respectively. The model was made of carbon fiber reinforced plastic shells to achieve high stiffness and low weight. The chord of the wind tunnel model is $c = 0.3$ m with a span of $s = 1$ m. The center of rotation of the airfoil model or the position of the elastic axis e is at $c/4$.

2.3 Sensors and data aquisition

To measure the model motion, pressure distributions and aerodynamic forces, both the test rig and the wind tunnel model were equipped with sensors. The angle α_{2D} of the 2D support was measured with four laser triangulators placed outside on both sides of the wind tunnel test section. Four additional laser triangulators, directly installed on the flutter test rig (see Fig. 2), were used to measure the relative angular twist of the wind tunnel model with respect to the 2D support. The addition of these two angles yields the time-resolved angle of attack $\alpha(t)$ of the airfoil with respect to the inflow. In addition, the heave motion $h(t)$ of the model was calculated from the laser signals. The error of the angle of attack is of the order of $\sigma_\alpha < \mathcal{O}(10^{-1})^\circ$, the error for the heave motion is slightly smaller with an order of $\sigma_h < \mathcal{O}(10^{-4})$ m. It should be noted that additional motion components due to structural deformations were not captured by the lasers.

For this purpose, the wind tunnel model is equipped with six accelerometers of the type PCB 35C22. The sensors are uniformly positioned along the leading edge and the trailing edge, $x/c \approx 0.1$ and $x/c \approx 0.8$ respectively, across the span at $0.06\ s$, $0.5\ s$, and $0.94\ s$. By integrating the acceleration signals twice in the frequency domain, the unsteady parts of the model motion in the midsection, divided into heave $\Delta h(t)$ and pitch $\Delta\alpha(t)$, were calculated. These also include the additional motion components of a structural model deformation.

Furthermore, the NLR7301 model is equipped with 64 unsteady differential pressure transducers of the type Kulite XCQ-093-5psiD to measure steady and unsteady pressure distributions. The pressure taps are staggered by ± 0.5 % span around the midsection of the wind tunnel model, the sensor distribution along the chord is shown in Fig. 3. Seven sensors exhibited a sharp drop in signal-to-noise ratio during the test campaign, so they were not used for data evaluation. These are represented by gray markers in Fig. 3. Aerodynamic forces and moments were obtained by integrating the measured pressure distributions in chord and spanwise direction. For this purpose, the pressure distributions were interpolated by cubic splines, in particular to close the missing sampling points of the failed sensors. For the final integration, a zero load assumption was made at the trailing edge, so that the Kutta condition was fulfilled.

The sensor signals as well as the wind tunnel data including flow parameters were recorded and preprocessed with the AMIS III data acquisition system of DLR-AE. The system is capable of simultaneously sampling the signals of ~ 1000 channels with up to 200 kHz per channel and 24 bit resolution. In the present test campaign, the signals were recorded at 1.2 kHz. Post-processing of the data was then done using MATLAB®.

2.4 Test parameters and methodology

Measurements were performed for Mach-numbers of $0.6 \leq \mathrm{Ma}_\infty \leq 0.79$ with a variable total pressure p_0 from 30 kPa up to 100 kPa. Thus, the chord based Reynolds-number Re_∞ varied from $1.1 \cdot 10^6$ to $3.54 \cdot 10^6$. For steady measurements, the mean angle of attack α_0 was set between $-2.0°$ to $2.9°$, flutter tests were performed for a mainly constant value of $0.4°$.

Both flutter tests and steady aerodynamic force measurements were carried out for a free transitional and a fully turbulent boundary layer. For this, the position x_{tr} of the boundary layer transition was fixed at $0.07c$ on the suction site and at $0.14c$ on the pressure site of the NLR7301 airfoil model, using transition tripping dots (0.183 mm height). While the flow parameters were set to constant values, identical measurements of the aerodynamic forces and the aeroelastic stability limits provide a direct comparison with respect to the influence of laminarity on the aerodynamic and aeroelastic behavior of the NLR7301 airfoil.

3 STRUCTURAL PROPERTIES OF THE AEROELASTIC SYSTEM

Prior to the flutter test, the structural parameters of the flutter test rig as well as of the wind tunnel model were determined by static and dynamic deflection tests. Frequencies and the damping of the natural modes of the aeroelastic system were obtained within the scope of a vibration test. For this purpose, the wind tunnel model and flutter test rig were equipped with additional acceleration sensors, 19 in total. The corresponding power spectral densities (PSDs) are shown in the center of Fig. 4, the rigid-body modes are depicted at the top, and the structural modes are illustrated at the bottom. The natural frequencies of the two experimentally specified rigid-body modes heave and pitch are $f_h = 29.3$ Hz and $f_\alpha = 54.4$ Hz, respectively. The corresponding damping coefficients (Lehr's damping coefficients) are $D_h = 0,65$ % and $D_\alpha = 0,20$ %. The error of the natural frequencies is negligible, whereas for the estimation of the damping a much larger error has to be assumed, comparable to the remarks in [12]. The rigid body roll mode with a frequency of $f_r = 35.5$ Hz is an artifact of the symmetric model suspension with no further significance for the flutter system. The additional structural modes have significantly higher natural frequencies and are clearly separated from the frequencies of the classical bending-torsion flutter system. All other relevant structural parameters, such as the total oscillating mass m, the moment of inertia with respect to the elastic axis I_α, the static mass moment S_α, the distance x_α of the center of gravity cg to the elastic axis position e and the stiffness of the heave and torsion spring system $k_h = m \cdot {\omega_h}^2$ and $k_\alpha = I_\alpha \cdot {\omega_\alpha}^2$ are summarized in Tab. 1. Based on results of static deflection tests, the structure can be considered as statically linear.

By optimizing individual components of the flutter test rig, the total oscillating mass and thus

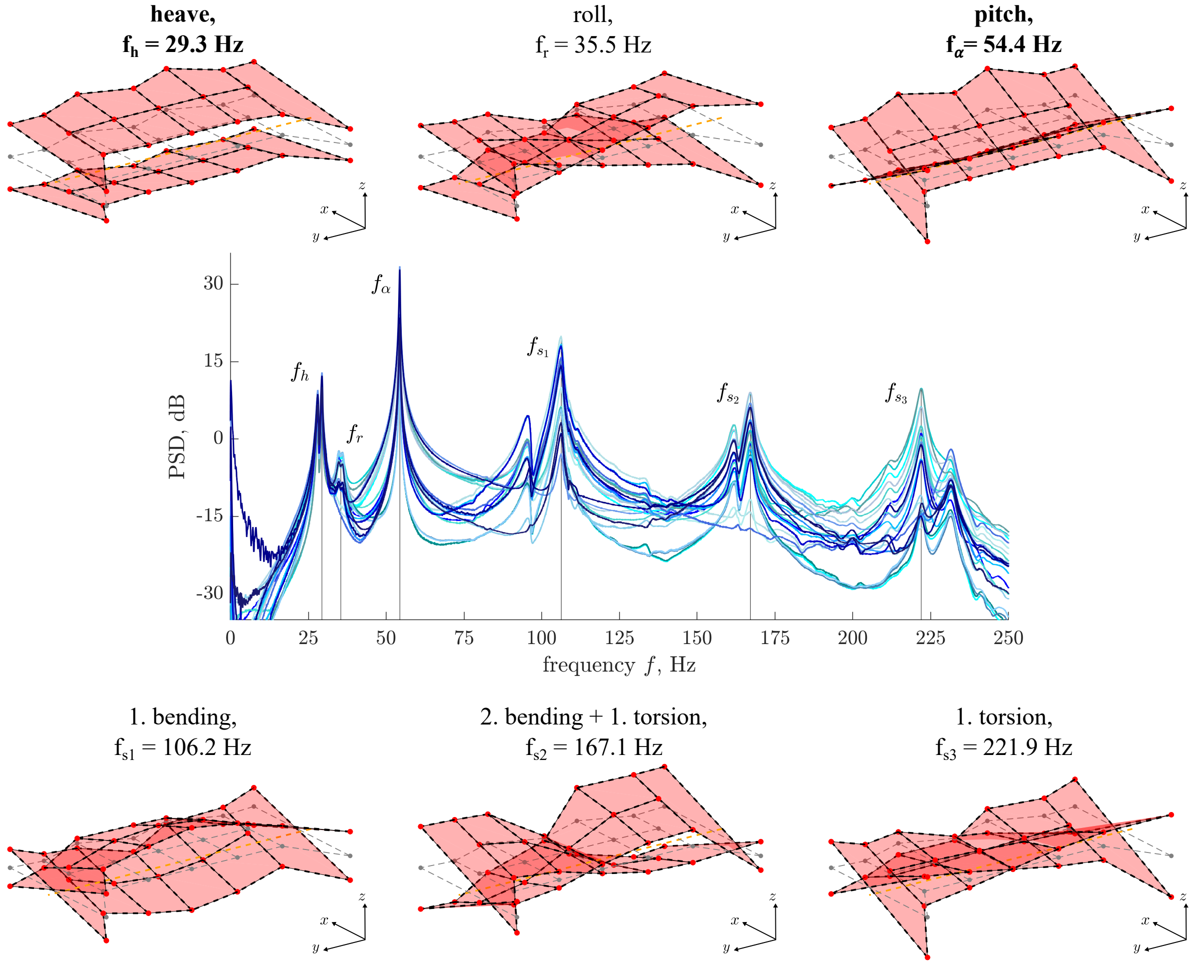

Figure 4: Natural frequencies and natural modes of the experimental setup (flutter test rig and NLR7301 wind tunnel model) identified during a vibration test.

the mass ratio $\mu = \frac{4m}{\pi c^2 s}/\rho_\infty$, which describes the ratio of the inertial forces to the aerodynamic loads, could be reduced by about 25 % compared to previous investigations [12]. The moment of inertia was reduced by about 50 %.

Table 1: Structural parameters of the aeroelastic system including the flutter test rig and the NLR7301 model.

parameter	**notation**	**unit**	**value**
total oscillating mass	m	kg	22,68
moment of inertia w.r.t. e	I_α	10^{-3} kg·m^2	60,13
static mass moment	S_α	kg·m	0,275
distance cg to e	x_α	m	0,012
heave stiffness	k_h	kN/m	$768,7$
pitch stiffness	k_α	Nm/rad	7025

4 RESULTS AND FINDINGS

4.1 Influence of laminarity on steady aerodynamics

For the measurement of the steady-state aerodynamic forces, the NLR7301 airfoil was fixed with the pneumatic brake of the flutter test rig while the angle of attack was varied by rotating the 2D support (cf. Sec. 2.1). Fixing the model ensures a completely stiff test setup without elastic model oscillations.

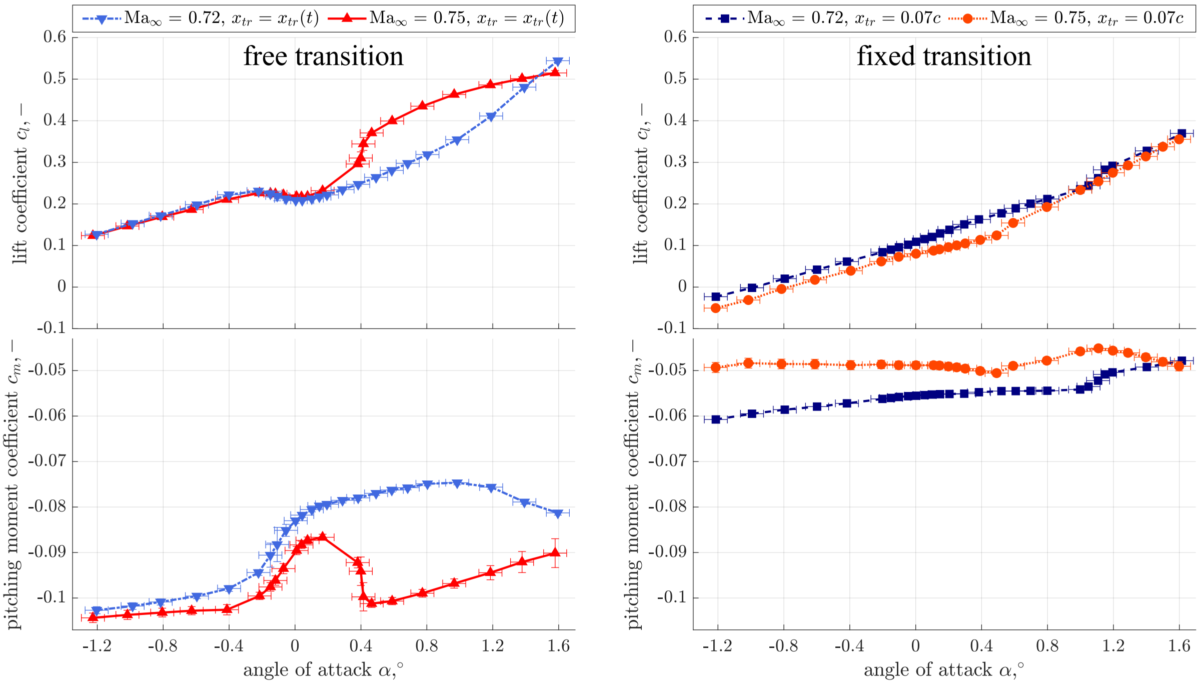

(a) free boundary layer transition, $x_{tr} = x_{tr}(t)$ (b) fixed boundary layer transition, $x_{tr} = 0.07c$

Figure 5: Steady lift $c_l(\alpha)$ and pitching moment $c_m(\alpha)$ curves for a free (a) and a fixed boundary layer transition (b) of the NLR7301 airfoil. The measurements were performed at a total pressure of $p_0 = 44$ kPa and Mach-numbers of $\mathrm{Ma}_\infty = [0.72, 0.75]$, resulting in Reynolds-numbers of about $\mathrm{Re}_\infty \approx 1.62 \cdot 10^6$ to $1.65 \cdot 10^6$.

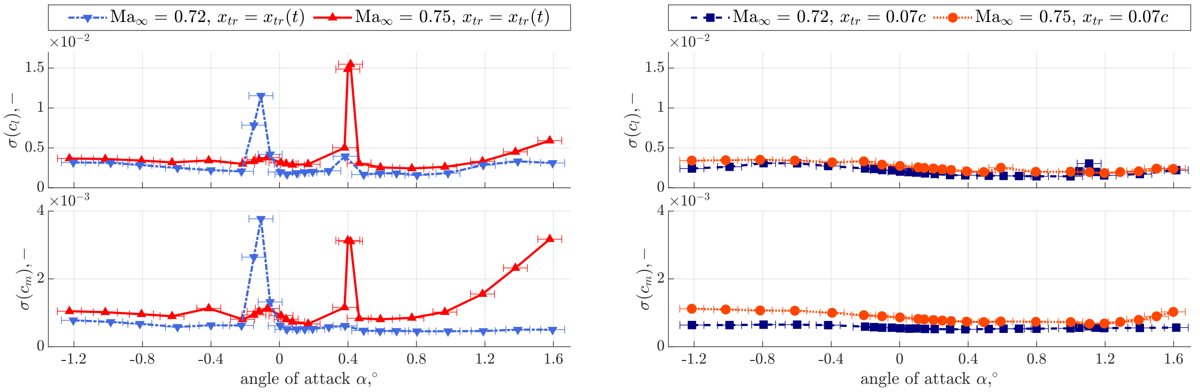

(a) free boundary layer transition, $x_{tr} = x_{tr}(t)$ (b) fixed boundary layer transition, $x_{tr} = 0.07c$

Figure 6: Standard deviations σ_{c_l} and σ_{c_m} of the lift and pitching moment coefficients shown in Fig. 5 for a free (a) and a fixed boundary layer transition (b).

In Fig. 5, the curves of the lift (top) and pitching moment (bottom) coefficients c_l and c_m versus the angle of attack α are shown for a free (left) and a fixed (right) boundary layer transition for Mach-numbers of $\mathrm{Ma}_\infty = 0.72$ and 0.75. The horizontal error bars correspond to the error of the mean angle of attack estimated with $\sigma_\alpha = 0.07°$, the vertical bars reflect the single standard deviations σ_{c_l} and σ_{c_m}, respectively. These are depicted again separately in Fig. 6. As Fig. 5(a) shows, aerodynamic nonlinearities appear for a free boundary layer transition, which are comparable to those of the CAST 10-2 laminar airfoil [2, 3]. A lift plateau $c_l \approx const.$ is formed around $\alpha_0 \approx 0°$, which corresponds to the upper transition region of a laminar drag bucket in the polar diagram of the NLR7301 airfoil. The NLR7301 airfoil thus shows characteristics of a laminar airfoil at Reynolds-numbers of $\mathrm{Re}_\infty \approx 1.6 \cdot 10^6$. It can also be clearly seen that a strong variation of the pitching moment coefficient c_m occurs in this transition region. This significant change in pitching moment is accompanied by locally increasing fluctuations of the aerodynamic forces, as shown by the increased standard deviations σ_{c_l} and σ_{c_m} in Fig. 6(a) for $\mathrm{Ma}_\infty = 0.72$ at $\alpha = -0.1°$ and for $\mathrm{Ma}_\infty = 0.75$ at $\alpha = 0.4°$.

A comparison of the aerodynamic coefficients and the corresponding standard deviations for a fixed transition, shown in Fig. 5(b) and Fig. 6(b), respectively, indicates that the observed nonlinearities and also the aerodynamic fluctuations are associated with the laminar-turbulent boundary layer transition and/or a shock-boundary layer interaction affiliated with it. Aerodynamic nonlinearities are significantly reduced for a turbulent boundary layer. As expected, the characteristics of a laminar drag bucket disappear completely in the curves of the aerodynamic coefficients. The aerodynamic fluctuations are also greatly reduced by an order of magnitude, with local increases around $\alpha = -0.1°$ and $\alpha = 0.4°$ disappearing as well.

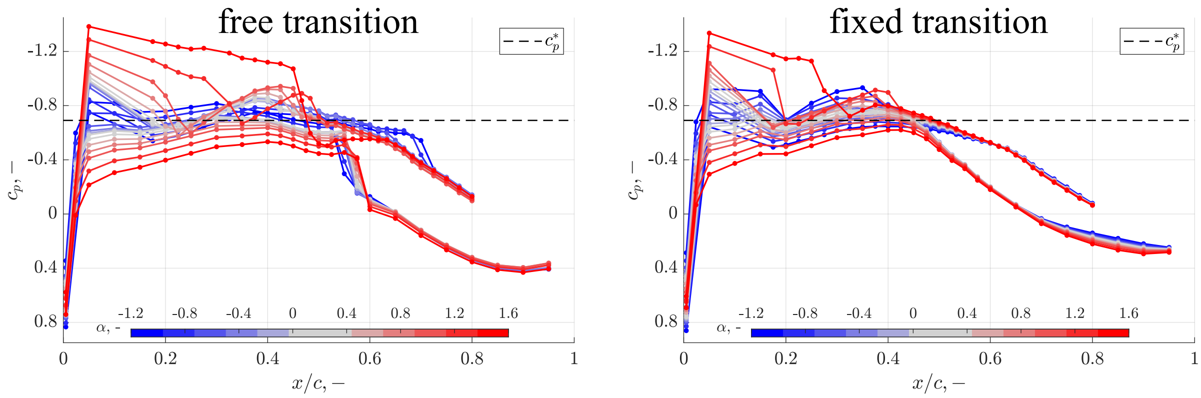

(a) c_p for $\mathrm{Ma}_\infty = 0.72$, $x_{tr} = x_{tr}(t)$ (b) c_p for $\mathrm{Ma}_\infty = 0.72$, $x_{tr} = 0.07c$

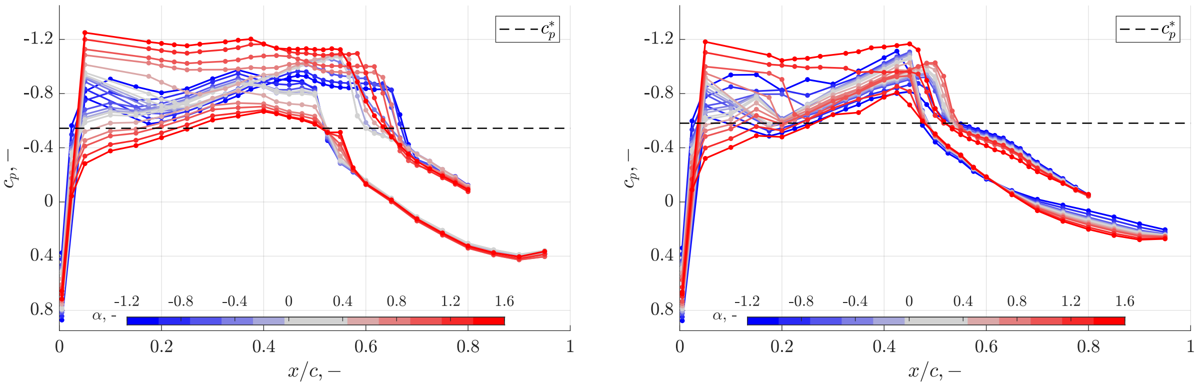

(c) c_p for $\mathrm{Ma}_\infty = 0.75$, $x_{tr} = x_{tr}(t)$ (d) c_p for $\mathrm{Ma}_\infty = 0.75$, $x_{tr} = 0.07c$

Figure 7: Pressure distributions for the measured aerodynamic force and moment curves at $p_0 = 44$ kPa for a free transitional and a turbulent boundary layer for Mach-numbers of $\mathrm{Ma}_\infty = 0.72$ in (a) and (b) and for $\mathrm{Ma}_\infty = 0.75$ in (c) and (d).

Fig. 7 shows the corresponding pressure distributions to the force and moment curves shown in Fig. 5. The dashed line marks the critical pressure coefficient c_p^*. Regardless of the state of the boundary layer, the supersonic region on the airfoil suction side increases with increasing Mach-number. A comparable effect is also seen at constant Mach-number between a fixed and a free transition. For $x_{tr} = x_{tr}(t)$ (Fig. 7(a) and (c)), the supersonic regions are more extended at the same angles of attack. Compression shocks occur further downstream than for $x_{tr} = 0.07c$ (Fig. 7(b) and (d)). These extended supersonic regions downstream of the elastic axes location in combination with higher pressures in the trailing edge region lead to higher trailing edge loads, higher lift coefficients and lower pitching moments for a free transition (cf. Fig. 5). This difference is due to a de-cambering of the effective airfoil contour as a result of the thickening associated with a turbulent boundary layer.

Compression shocks occur on the airfoil suction side as a function of Mach-number and angle of attack for all four cases. The pressure side, however, remains shock-free for $\mathrm{Ma}_\infty = 0.72$, for $\mathrm{Ma}_\infty = 0.75$ shocks occur around $0.5 \leq x/c \leq 0.55$. Furthermore, the pressure rises localized there coincide with the boundary layer transition for $x_{tr} = x_{tr}(t)$. The same applies to the compressions at $\mathrm{Ma}_\infty = 0.72$, analogous to results for the CAST 10-2 laminar airfoil [7, 8]. The transition position is stationary on the pressure side and largely independent of the angle of attack. Aerodynamic nonlinearities and characteristics thus result primarily from the flow phenomena along the airfoil suction side.

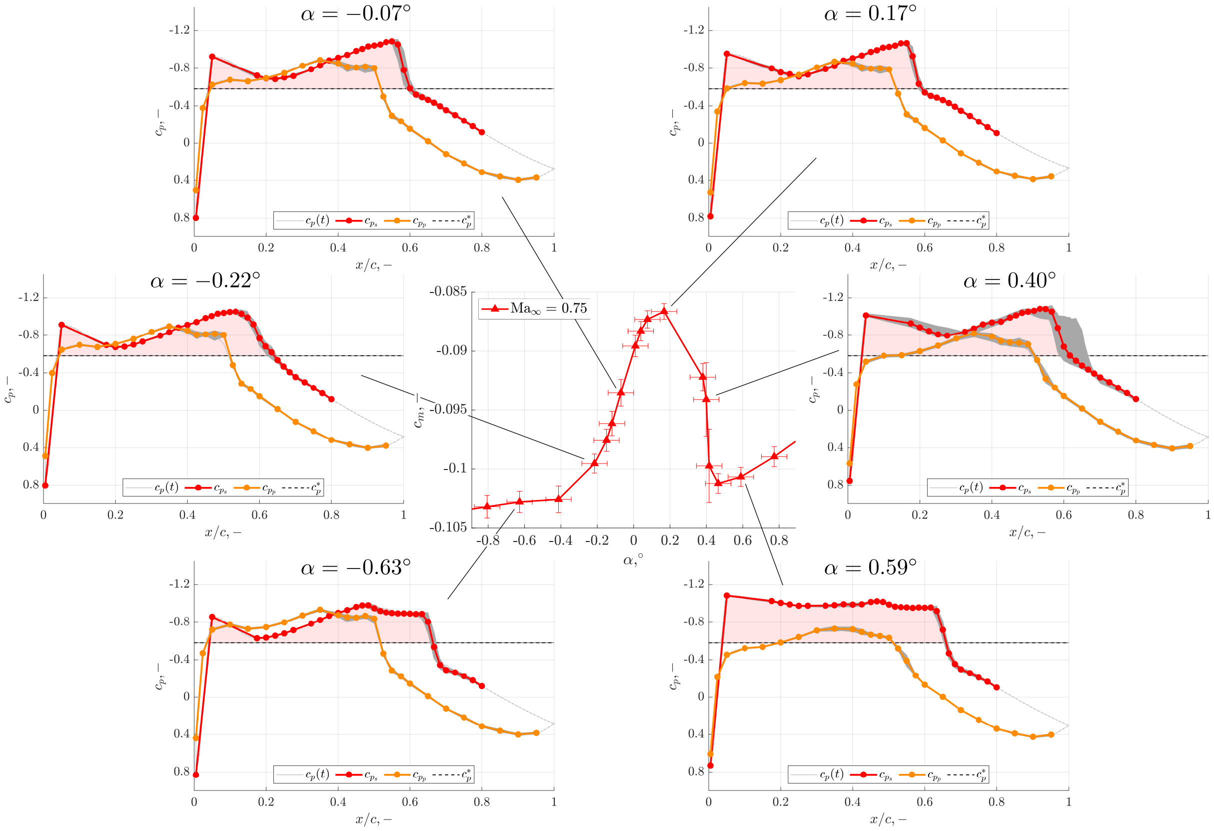

Figure 8: Pressure distributions for selected angles of attack along the moment profile $c_m(\alpha)$ for $\mathrm{Ma}_\infty = 0.75$ and a free boundary layer transition $x_{tr} = x_{tr}(t)$.

To illustrate these phenomena, Fig. 8 again shows individual pressure distributions at the prominent points in the pitching moment curve for $x_{tr} = x_{tr}(t)$ and $\mathrm{Ma}_\infty = 0.75$. Within the laminar drag bucket for $\alpha = -0.63°$, the pressure distribution indicates a laminar running length of more than 50% of the chord. The pressure plateau at $x/c \approx 0.65$ indicates a shock-boundary layer interaction with formation of a laminar separation bubble. Consequently, although there is already a pressure increase around $x/c \approx 0.1$, the renewed flow expansion is sufficient to stabilize the laminar boundary layer and move the transition downstream until the compression shock. As the angle of attack increases, the supersonic area in the front part of the airfoil grows. The shock moves inversely upstream. The lift at the front increases, which becomes clear in the rise of the pitching moment for $-0.4° \leq \alpha \leq 0.2°$. The pressure increase associated with the shock initially weakens for $\alpha = -0.22°$, but steepens again for $\alpha = -0.07°$ and $\alpha = 0.17°$.

A further increase of the angle of attack beyond $\alpha \approx 0.2°$ then leads to a rather abrupt movement of the compression shock downstream and an increase of the suction peak. This explains the sharp drop in pitching moment. The position of the compression shock is sensitive to a change in the angle of attack, as shown by the unsteady pressure distribution $c_p(t)$ (gray background) for $\alpha = 0.40°$. For $\alpha = 0.59°$ the shock position is then steady and downstream shifted, comparable to $\alpha = -0.63°$. A further increase of the angle of attack then leads to a continuous growth of the supersonic region and an inverse shock movement, as shown in Fig. 7(c).

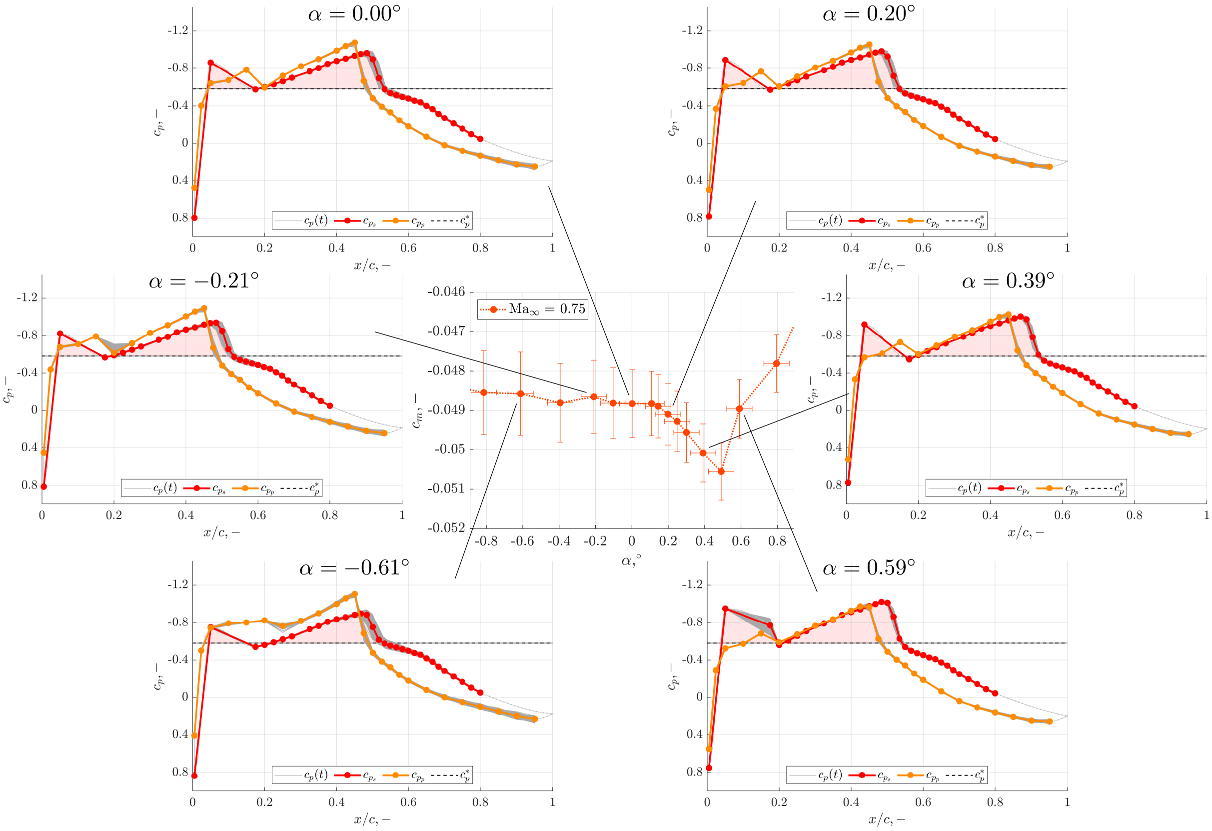

Figure 9: Pressure distributions for selected angles of attack along the moment profile $c_m(\alpha)$ for $\mathrm{Ma}_\infty = 0.75$ and a fixed boundary layer transition $x_{tr} = 0.07c$.

In Fig. 9 the moment curve including pressure distributions for a fixed boundary layer transition $x_{tr} = 0.07c$ is shown for direct comparison. With increasing angle of attack, there is a continuous growth of the supersonic regions and an increasingly steep pressure rise in the range $x/c \approx 0.55$. The shock strength increases accordingly, although the shock position remains largely stationary over the entire range of angles of attack shown. Compared to the free boundary layer transition, the supersonic regions are smaller overall and partially interrupted by a pressure increase following downstream of the suction peak. For $x_{tr} = x_{tr}(t)$ this is also present, but decreases with increasing angle of attack and disappears for $\alpha \approx 0.6°$. In direct comparison, for a fixed boundary layer transition, the pressure increase becomes stronger and forms another compression shock at $\alpha = 0.59°$. There is a double shock system for this angle of attack range. With a further increase of α both supersonic regions merge into each other and the double shock system disappears. This is also reflected in the triangular shape of the pitching moment (cf. Fig. 5(b)) for $0.2° \leq \alpha \leq 1.6°$. Overall, changes in the pressure distribution with changing angle of attack for a fixed transition are moderate and do not exhibit pronounced aerodynamic instationarities. Thus, no significant nonlinearities or large steady force or moment derivatives appear in the integral coefficients.

The influence of the boundary layer state on the overall flow field around the NLR7301 profile thus results from different shock-boundary layer interactions with a laminar/transitional or tubulent boundary layer, as the direct comparison of Fig. 8 with Fig. 9 shows. Clearly altered shock strengths and shock dynamics occur, which is directly reflected in the course of the coefficients and, in particular, in the gradients or steady derivatives.

4.2 Unsteady effects and aerodynamic limit cycle oscillations

As already mentioned in 4.1, unsteady effects already occur for fixed angles of attack at the NLR 7301 airfoil in case of a free boundary layer transition (cf. Fig. 6(a)). For a more detailed explanation, Fig. 10 shows the pressure distribution as well as the PSD of the pressure distribution of the airfoil suction side for $\mathrm{Ma}_\infty = 0.72$ and $\alpha = -0.1°$.

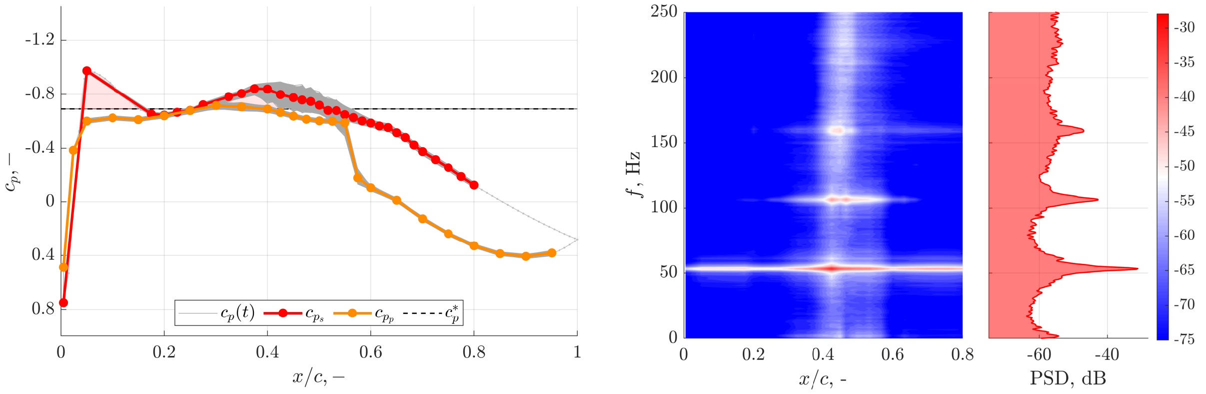

(a) c_p und $c_p(t)$

(b) PSD(c_{p_s})

Figure 10: Averaged and time-resolved pressure distribution c_p and $c_p(t)$ (a) and associated PSD of the pressure distribution of the airfoil suction side PSD(c_{p_s}) (b) for $\mathrm{Ma}_\infty = 0.72$, $\alpha = -0.1°$, and $x_{tr} = x_{tr}(t)$.

The pressure distribution shows that no compression shock occurs for this angle of attack. The pressure increase in the front region of the airfoil chord corresponds to a shock-free recompression which does not show any unsteadiness. Temporal changes in the pressure distribution, on the other hand, occur at $0.4 \leq x/c \leq 0.6$, as shown by the gray shaded area in Fig. 10(a). These fluctuations show clear harmonic components, as the PSD in Fig. 10(b) illustrates. Spectral components with a frequency of 53.3 Hz appear in the range already mentioned above. In addition, the first and second higher harmonics are also recognizable.

This has a direct effect on the aerodynamic coefficients. Fig. 11 shows the corresponding time series of lift $c_l(t)$ and pitching moment $c_m(t)$ together with a phase space representation and the respective PSDs. The harmonic oscillations in the pressure distribution are transferred to the integral coefficients. In particular, the phase space plots illustrate that aerodynamic LCOs occur. These excite the model structure, however, with a standard deviation of $\sigma_{\Delta h} < 0.04$ mm for the heave and $\sigma_{\Delta\alpha} < 0.01°$ for the pitch component, the structural motions induced in the midsection of the wind tunnel model are in an aerodynamically negligible range. According to the trend of $c_m(\alpha)$ at $\mathrm{Ma}_\infty = 0.72$ (cf. Fig. 5(a)), an angle of attack variation of $\Delta\alpha \approx 0.15°$ would be required around $\alpha = -0.1°$ to produce a comparable change of $\Delta c_m \approx 0.01$ as occurs for the aerodynamic LCO. Thus, it can be assumed that a self-excited oscillation of the fluid and no structure-induced response is present. Furthermore, wind tunnel resonances can be excluded with the estimation according to [15, 16].

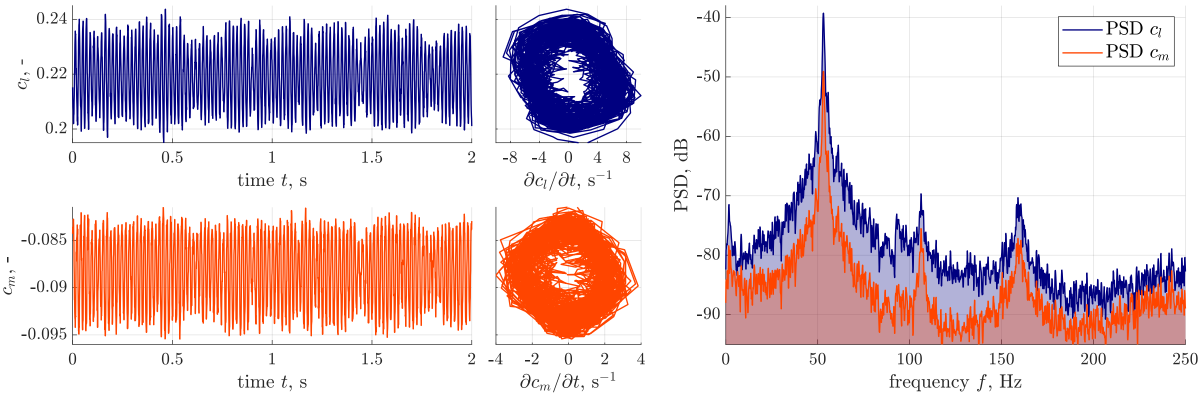

Figure 11: Time series, phase space representations, and auto-power density spectra of the lift and moment coefficients $c_l(t)$ and $c_m(t)$ for $\mathrm{Ma}_\infty = 0.72$, $\alpha = -0.1°$, and $x_{tr} = x_{tr}(t)$.

Comparable effects also occur at the CAST 10-2 laminar airfoil. Among other things, these were attributed to a self-excited, periodic oscillation of the position of the boundary layer transition, a transition buffet [9]. For the present measurement, no direct information about the boundary layer state is available, so that an oscillation of the boundary layer transition cannot be verified as a cause. However, a connection with a free boundary layer transition is clearly clarified. For a fixed transition, such aerodynamic instationarities do not occur. The other fluctuations occurring for $\alpha = 0.4°$ and $\mathrm{Ma}_\infty = 0.75$ (cf. Fig. 6(a) and pressure distribution in Fig. 8), on the other hand, do not exhibit harmonic or periodic components. This is a transient, intermittent shock motion downstream and a shock-boundary layer interaction with formation of a laminar separation bubble. However, there is also a direct connection to the free boundary layer transition.

4.3 Influence of laminarity on the transonic dip

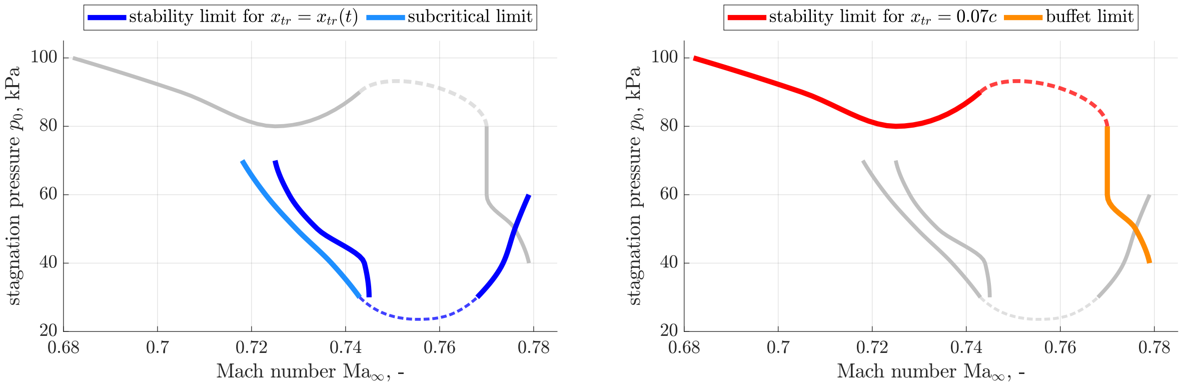

(a) stability limit for $x_{tr} = x_{tr}(t)$ (b) stability limit for $x_{tr} = 0.07c$

Figure 12: Aeroelastic stability limits for a free (a) and a fixed (b) boundary layer transition measured for a mean angle of attack of $\alpha_0 = 0.4°$. For comparison purposes, the other stability limit is shown in gray. The dashed lines are interpolated limits, since no measurements were made there.

The different progressions and fluctuations of the aerodynamic coefficients now also affect the aeroelastic behavior. Fig. 12 shows the aeroelastic stability limits of the NLR7301 airfoil measured during the flutter test for a mean angle of attack of $\alpha_0 = 0.4°$. Fig. 12(a) shows the stability limit for a free transitional boundary layer, in Fig. 12(b) the limit for a turbulent boundary layer is depicted. Thereby, the shift of the stability limit towards smaller total pressures for a free boundary layer transition is clearly evident for this angle of attack, as it has already been shown for the CAST 10-2 airfoil [4, 7–9].

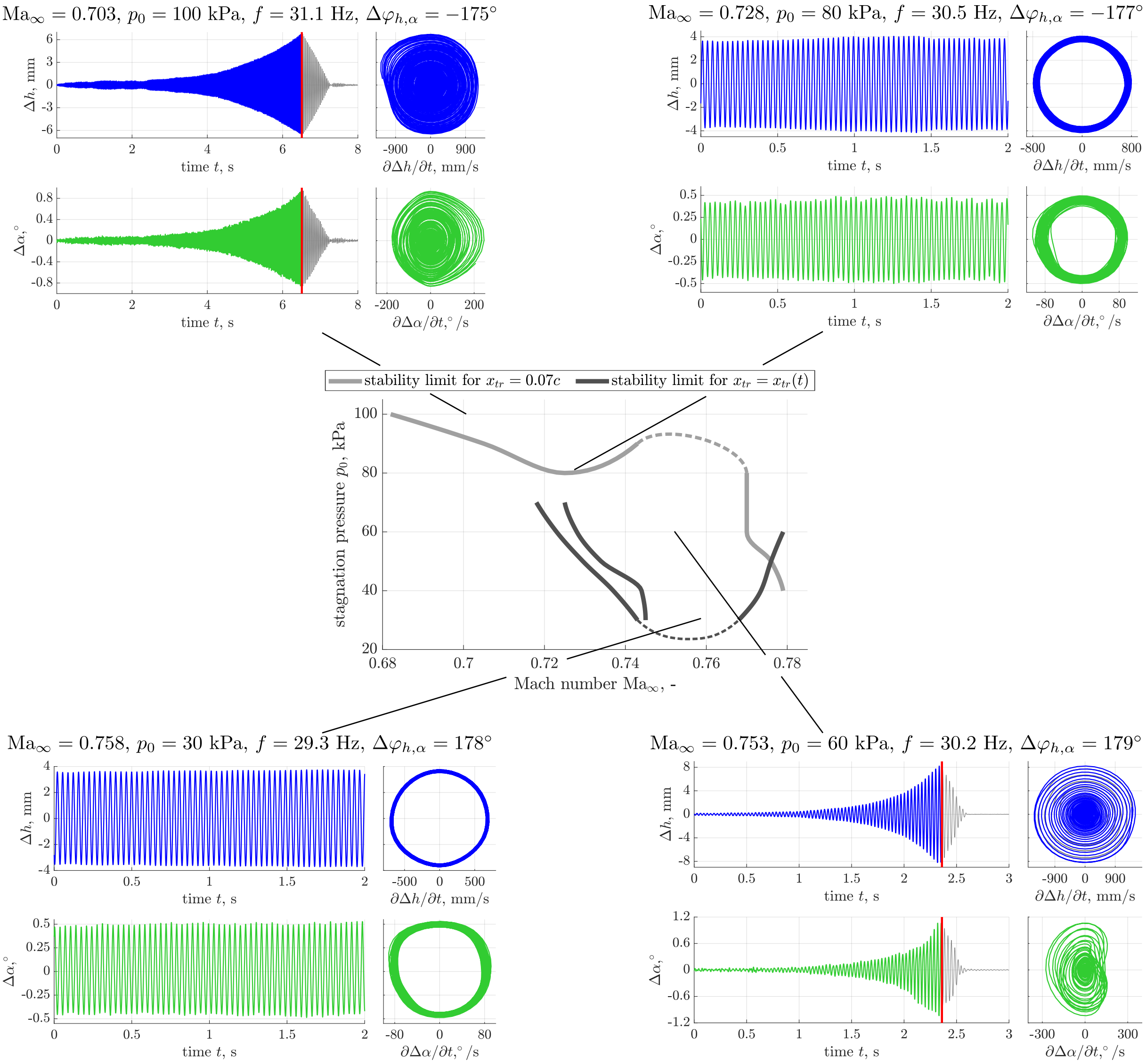

Figure 13: Illustration of exemplary flutter cases within the measured transonic dips. The upper time series correspond to the unstable region for a fixed transition, the lower time series to the dip as it occurs for a free transition. The corresponding flow and flutter parameters are entered above the time series.

Exemplary flutter cases as they occur in different regions of the determined transonic dips are shown in Fig. 13. The time series of the motion of the midsection of the wind tunnel model, divided into heave Δh and pitch $\Delta\alpha$, as well as the phase space representations are depicted. For both a turbulent and a free boundary layer transition, limit cycle oscillations occur in each case near the stability limit, especially at the bottom of the transonic dips. At higher pressures or higher Mach-numbers, however, the amplitudes of the self-excited model oscillations grow rapidly. Possible further limit cycles are here outside an experimentally still observable range. An uncontrolled increase of the amplitudes of such flutter cases was stopped by the pneumatic brake (cf. Sec. 2.1). This is marked by a red bar in the time series.

A comparison among each other shows that, independent of the boundary layer state, heave-dominated flutter cases occur with a flutter frequency f close to the experimentally specified natural frequency of the heave DoF $f_{h,0} = 29.3$ Hz (cf. Sec. 3). With increasing total pressure p_0 the flutter frequencies increase minimally from $f = 29.3$ Hz at $p_0 = 30$ kPa to $f = 31.1$ Hz at $p_0 = 100$ kPa. This indicates an additional aerodynamic stiffness contribution due to the pressure or density increase. Also the phase differences between the heave and the pitch motion hardly change. For all classical flutter cases these are in the range of $\Delta\varphi_{h,\alpha} \approx 180°$. According to previous studies, this can be interpreted as a single degree of freedom flutter about a virtually shifted axis of rotation [10–12].

The pronounced influence of the boundary layer state and the associated shift in the stability limit is clearly evident, analogous to the CAST 10-2 laminar airfoil. Deviating from the CAST 10-2 results discussed in [9], however, no additional boundary layer transition flutter occurs for a mean angle of attack of $\alpha = 0.4°$ investigated here, which would still complement and thus extend the dip as an additional flutter mechanism.

4.4 Further observed aeroelastic instabilities

In addition to the previously mentioned flutter cases, further aeroelastic instabilities occur, which are also partly influenced by the state of the boundary layer. As already illustrated by the additional stability limits in Fig. 12, subcritical flutter cases and buffeting, among others, were observed along the transonic dip. These cases are briefly explained below.

4.4.1 Subcritical flutter

Subcritical flutter cases are characterized by the fact that the flutter onset is described by a subcritical bifurcation. A self-excited oscillation is only triggered if an external disturbance with sufficient amplitude occurs. Such flutter cases have already been observed and described for the NLR7301 profile [10] as well as for the CAST 10-2 laminar airfoil [6].

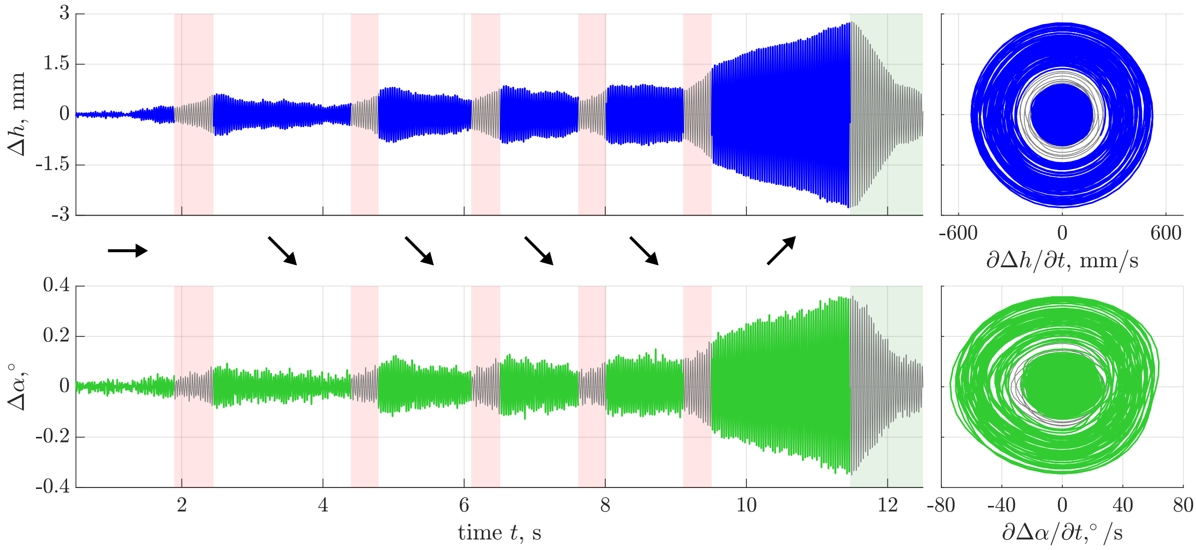

Figure 14: Time series and phase space representations for an exemplary subcritical flutter case recorded for $\mathrm{Ma}_\infty = 0.723$, $p_0 = 70$ kPa, $\alpha = 0.4°$, and $x_{tr} = x_{tr}(t)$.

The subcritical stability limit shown in Fig. 12 marks the onset of such flutter cases, which were observed in the entrance region of the transonic dip for both a fixed and a free boundary layer transition. For the latter case, subcritical flutter cases have been observed over a more extended

Mach-number range, so a separate stability limit has been drawn in Fig. 12. An exemplary case is depicted in Fig. 14. The areas highlighted in red mark time periods in which the heave DoF was excited using the electrodynamic exciters (see Sec. 2.1). The perturbation amplitude was increased several times until a self-excited growth of the oscillation amplitudes (illustrated by arrows in Fig. 14) occurred. Based on the gray inner circle in the phase space representations, the position of the repeller is well visible. In the area highlighted in green, the oscillation has been damped and the amplitudes have thus stopped rising.

Even if a direct connection with the state of the boundary layer is not recognizable, subcritical bifurcations nevertheless lead to an expansion of the unstable region, as Fig. 12(a) shows. Aeroelastic systems with consideration of a free boundary layer transition are inherently nonlinear. It is all the more likely that subcritical bifurcations will describe the onset of flutter in addition to supercritical ones. Both numerically and in the experiment, subcritical flutter cases must be explicitly searched for, since they are not observed with classical methods. Therefore, they represent an often overlooked aeroelastic risk whose importance will increase in aeroelastic system assessment incorporating boundary layer effects.

4.4.2 Buffeting

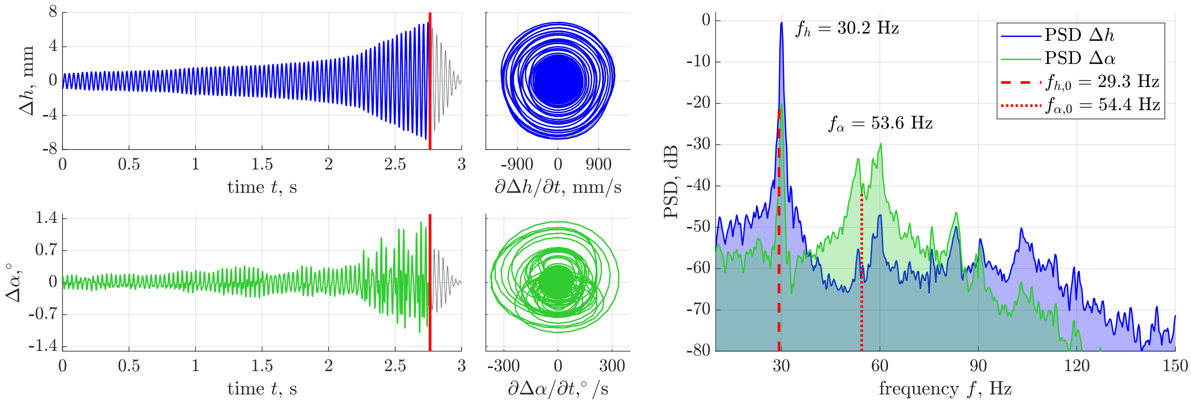

(a) Heave-dominated flutter case for $\mathrm{Ma}_\infty = 0.774$, $p_0 = 60$ kPa, $\alpha_0 = 0.4°$ and $x_{tr} = x_{tr}(t)$. The frequencies of the specified DoFs are shifted to $f_h = 30.2$ Hz and $f_\alpha = 53.6$ Hz, the phase difference is $\Delta\varphi_{h,\alpha}(f_h) = 179°$.

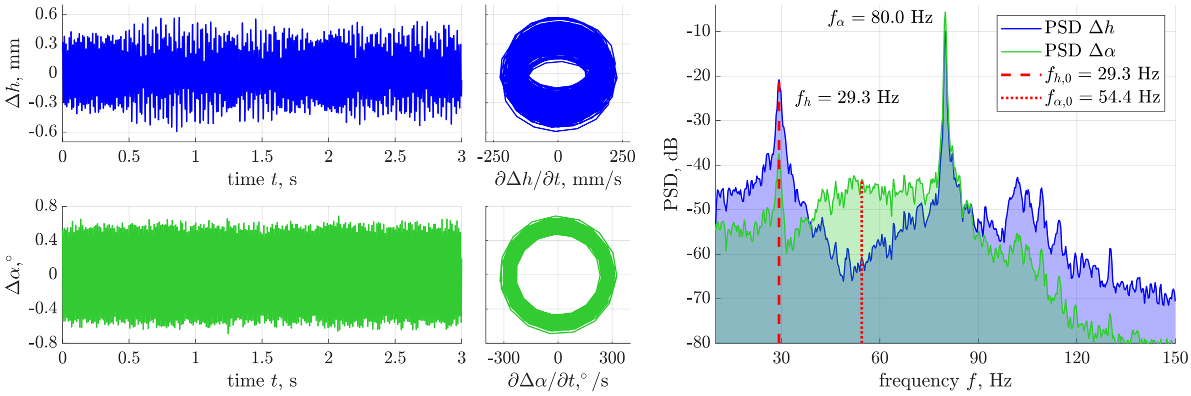

(b) Buffeting for $\mathrm{Ma}_\infty = 0.770$, $p_0 = 60$ kPa, $\alpha_0 = 0.4°$ and $x_{tr} = 0.07c$. The frequencies of the specified DoFs are shifted to $f_h = 29.3$ Hz and $f_\alpha = 80.0$ Hz, the phase difference is $\Delta\varphi_{h,\alpha}(f_\alpha) = -43°$.

Figure 15: Comparison of a classical flutter case for $x_{tr} = x_{tr}(t)$ (a) and buffeting for $x_{tr} = 0.07c$ (b) with otherwise nearly identical flow conditions.

At higher Mach-numbers, buffeting occurs for $x_{tr} = 0.07c$ in the investigated configuration. For $x_{tr} = x_{tr}(t)$, on the other hand, classical flutter occurs for comparable flow parameters.

Buffeting at free boundary layer transition up to a Mach-number of $\mathrm{Ma}_\infty = 0.785$ and $p_0 = 60$ kPa was not observed. A direct comparison of these two cases at nearly identical flow parameters of $\mathrm{Ma}_\infty \approx 0.77$ and $p_0 = 60$ kPa is shown in Fig. 15.

Fig. 15(a) shows a classical flutter case as it occurs for free transition and the flow parameters mentioned above. It has already been discussed in Sec. 4.3. The flutter frequency is $f = 30.2$ Hz, which is close to the heave-DoF natural frequency, as illustrated by the PSDs of Δh and $\Delta\alpha$. Fig. 15(b), on the other hand, shows an aeroelastic instability occurring for $x_{tr} = 0.07c$. Here, a pitch-dominated LCO with small amplitudes is present, which is significantly different from the classical flutter case. The frequency of the LCO is $f = 80.0$ Hz, which is clearly outside the frequency range given by the initial eigenfrequencies of the experimental flutter system. The phase difference between heave and pitch also deviates significantly from classical flutter with $\Delta\varphi_{h,\alpha}(f) = -43°$.

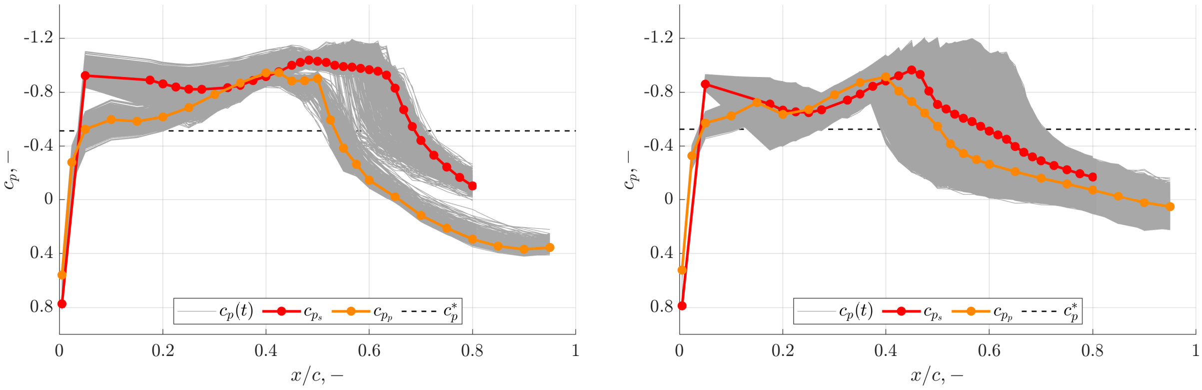

(a) pressure distribution $c_p(t)$ for $x_{tr} = x_{tr}(t)$ (b) pressure distribution $c_p(t)$ for $x_{tr} = 0.07c$

Figure 16: Pressure distributions for the flutter cases shown in Fig. 15. The colored curves represent the time average values, the gray areas mark the time-resolved pressure distributions for the three-second period shown in Fig. 15.

Fig. 16 shows the pressure distributions corresponding to Fig. 15. From this it is clear that shock buffeting occurs when the transition is fixed (Fig. 16(b)). On the suction side, the compression shock moves along an airfoil chord of $0.5 \leq x/c \leq 0.7$ during one oscillation period. On the pressure side, a shock movement takes place in the range of $0.4 \leq x/c \leq 0.55$. Thereby, the pressure distributions indicate separation regions on the suction side, which temporarily migrate upstream up to $x/c \approx 0.6$. Such shock dynamics are not present in the classical flutter case for $x_{tr} = x_{tr}(t)$ shown in Fig. 16(a), although the pitching amplitudes are more than twice as large. According to this, the state of the boundary layer not only affects the classical flutter behavior and the transonic dip, but also the buffet boundary is influenced. This underlines once more the necessity to include a free boundary layer transition also with respect to the estimation of buffet onset.

4.4.3 Boundary layer transition associated instability

In addition to the aeroelastic instabilities and flutter cases described so far, an additional aeroelastic instability was found solely for a free boundary layer transition at a slightly lower mean angle of attack of $\alpha_0 = -0.05°$, shown in Fig. 17. This aeroelastic instability is manifested by pitch dominated limit cycle oscillations with very small amplitudes and corresponds to the aerodynamic fluctuations as shown in Fig. 6(a) for $\mathrm{Ma}_\infty = 0.72$ around $\alpha_0 \approx -0.05°$. On the one hand, this instability is distinguished from the heave-dominated flatter cases (cf. Fig. 13

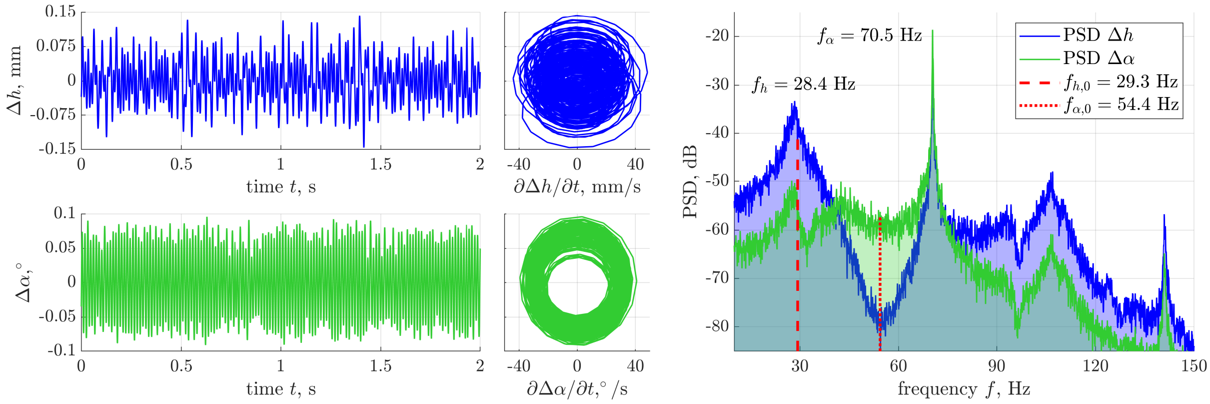

Figure 17: Aeroelastic instability for $\mathrm{Ma}_\infty = 0.722$, $p_0 = 44$ kPa, $\alpha_0 = -0.05°$ and $x_{tr} = x_{tr}(t)$. The frequencies of the specified DoFs are shifted to $f_h = 28.4$ Hz and $f_\alpha = 70.5$ Hz, the phase difference is $\Delta\varphi_{h,\alpha}(f_\alpha) = -57°$.

and 15(a)) by the high oscillation frequencies of $f_\alpha = 70.5$ Hz. On the other hand, this case is strongly limited to small angles of attack and low Mach-numbers where no shock buffet (cf. Fig. 15(b)) occurs yet. The pressure distribution corresponding to this instability is largely identical to that shown in Fig. 10(a). Analogous to the unsteady effects as described in Sec. 4.2, no direct information about the boundary layer behavior is available. A connection between this aeroelastic instability and a periodic motion of the boundary layer transition can therefore not be verified.

Nevertheless, clear analogies can also be seen in this case at the NLR7301 airfoil to the aerodynamic and aeroelastic instabilities of the CAST 10-2 laminar airfoil. There, these instabilities were identified as novel boundary layer transition flutter and boundary layer transition buffet cases [9]. Accordingly, it can be assumed that additional aeroelastic instabilities induced by a free boundary transition also occur for the NLR7301 airfoil.

5 CONCLUSIONS

The results of the flutter experiment performed with the supercritical NLR7301 airfoil demonstrate that laminarity or a freely moving boundary layer transition leads to comparable aerodynamic and aeroelastic effects as already observed and described for the CAST 10-2 supercritical laminar airfoil.

Also for the NLR7301 profile, nonlinear aerodynamic coefficient trends occur due to a free boundary layer transition, which in turn lead to local, strongly increased gradients or steady derivatives. This is accompanied by instationarities, some of which lead to aerodynamic LCOs. From an aeroelastic point of view, for an mean angle of attack of $\alpha = 0.4°$, which correlates with such a steep gradient $\partial c_m/\partial\alpha < 0$, it is shown that the flutter limit is lowered. A free boundary layer transition results in a shift of the transonic dip towards significantly lower total pressures. Compared to the CAST 10-2 airfoil, however, no additional flutter cases occur within the transonic dip for this investigated angle of attack. Nevertheless, in the marginal areas of the dip there are indications that, in addition to subcritical flutter cases, buffeting and the buffet boundary are also influenced by the state of the boundary layer. Additional aeroelastic instabilities, on the other hand, occur for an angle of attack around $\alpha = -0.05°$, where a connection to the aerodynamic LCOs can be assumed. It is reasonable to assume that these instabilities are induced with or by a free boundary layer transition, since they disappear when the boundary layer is fully turbulent.

The investigations on the influence of laminarity on the aeroelastic behavior of the NLR7301 airfoil confirm that the effects initially observed for the CAST 10-2 laminar airfoil are not exclusively profile-specific. The NLR7301 profile also exhibits comparable effects in the case of a free boundary layer transition. Hence, it follows that a general risk potential for aeroelastic instabilities is associated with the state of the boundary layer. An aeroelastic risk assessment must include a free boundary layer transition, especially for evaluating future laminar airfoil configurations.

6 REFERENCES

[1] Tichy, L., Mai, H., Fehrs, M., et al. (2017). Risk analysis for flutter of laminar wings. In *International Forum on Aeroelasticity and Structural Dynamics (IFASD), 25-28 June, Como, Italy.*

[2] Hebler, A., Schojda, L., and Mai, H. (2013). Experimental investigation of the aeroelastic behaviour of a laminar airfoil in transonic flow. In *International Forum on Aeroelasticity and Structural Dynamics (IFASD), 24-26 June, Bristol, United Kingdom.*

[3] Braune, M. and Hebler, A. (2018). Experimental investigation of transonic flow effects on a laminar airfoil leading to limit cycle oscillations. In *Applied Aerodynamics Conference, AIAA AVIATION Forum, June 25-29, Atlanta, Georgia.* doi:10.2514/6.2018-3641.

[4] Hebler, A. (2017). Experimental assessment of the flutter stability of a laminar airfoil in transonic flow. In *International Forum on Aeroelasticity and Structural Dynamics (IFASD), 25-28 June, Como, Italy.*

[5] Braune, M. and Hebler, A. (2019). Mechanisms of Transonic Single Degree of Freedom Flutter of a Laminar Airfoil. In *International Forum on Aeroelasticity and Structural Dynamics (IFASD), 9-13 June, Savannah, Georgia, USA.*

[6] Braune, M. and Hebler, A. (2019). Hysteretic response of a laminar airfoil undergoing single degree of freedom limit cycle oscillations in transonic flow. In *International Forum on Aeroelasticity and Structural Dynamics (IFASD), 9-13 June, Savannah, Georgia, USA.*

[7] Fehrs, M. (2013). Influence of transitional flows at transonic mach numbers on the flutter speed of a laminar airfoil. In *International Forum on Aeroelasticity and Structural Dynamics (IFASD), 24-26 June, Bristol, United Kingdom.*

[8] Fehrs, M., van Rooij, A. C. L. M., and Nitzsche, J. (2015). Influence of boundary layer transition on the flutter behavior of a supercritical airfoil. *CEAS Aeronautical Journal*, 6(2), 291–303. doi:10.1007/s13272-014-0147-7.

[9] Braune, M. (2021). *Identification of a flutter mechanism on a supercritical airfoil with laminar flow*. Ph.D. thesis, Georg-August-Universität Göttingen. Available in german.

[10] Schewe, G., Mai, H., and Dietz, G. (2003). Nonlinear effects in transonic flutter with emphasis on manifestations of limit cycle oscillations. *Journal of Fluids and Structures*, 18(1), 3–22. doi:10.1016/S0889-9746(03)00085-9.

[11] Dietz, G., Schewe, G., and Mai, H. (2004). Experiments on heave/pitch limit-cycle oscillations of a supercritical airfoil close to the transonic dip. *Journal of Fluids and Structures*, 19, 1–16. doi: 10.1016/j.jfluidstructs.2003.07.019.

[12] Dietz, G., Schewe, G., and Mai, H. (2006). Amplification and amplitude limitation of heave/pitch limit-cycle oscillations close to the transonic dip. *Journal of Fluids and Structures*, 22(4), 505–527. doi: 10.1016/j.jfluidstructs.2006.01.004.

[13] Wedemeyer, E., Taylor, N. J., and Holst, H. (1998). Adaptive wall techniques. In B. Ewald (Ed.), *Wind Tunnel Wall Corrections*, AGARD-AG-336, chap. 10. Advisory Group for Aerospace Research & Development, pp. 1–48.

[14] Zwaan, R. (1979). Summary of data required for the AGARD SMP activity 'Standard Aeroelastic Configurations' - two dimensional configurations. Tech. Rep. NLR MP 79015 U, Nationaal Lucht- en Ruimtevaartlaboratorium.

[15] Runyan, H. L., Woolston, D. S., and Rainey, A. G. (1955). Theoretical and experimental investigation of the effect of tunnel walls on the forces on an oscillating airfoil in two-dimensional subsonic compressible flow. Technical Note 3416, National Advisory Commitee for Aeronautics.

[16] Voss, R. (1998). Wind tunnel wall corrections. Report 336, AGARD.

COPYRIGHT STATEMENT